Benchmarking Signorini and exponential contact laws for an industrial train brake squeal application

Guillaume Vermot Des Roches, Olivier Chiello, Etienne Balmès, Xavier Lorang

Benchmarking Signorini and exponential contact laws for an industrial train brake squeal application

G. Vermot des Roches [1,2], **O. Chiello** [3,4], **E. Balmes** [1,2], **X. Lorang** [5]
[1]SDTools
44 rue Vergniaud, F-75013, Paris, France
e-mail: **vermot@sdtools.com**

[2]Arts et Metiers ParisTech
151 Boulevard de l'Hôpital, F-75013, Paris, France

[3]IFSTTAR-LTE
25 avenue François Mitterrand, F-69675, Bron, France

[4]Centre Lyonnais d'Acoustique (CeLyA)
Université de Lyon, F-69622 Lyon, France

[5]SNCF, Innovative and Research department
40 avenue des terroirs de France, F-75611, Paris, France

Abstract
Contact and friction play a key role in many industrial applications and their modeling is becoming accessible in vibration applications. Two strategies are commonly considered: idealized or perfect contact which assumes no interpenetration of structures at contact points and functional representations that use pressure-penetration relationships. The two strategies imply widely different solvers so that the choice between the two is almost always based on *a priori* decisions. For an application to the prediction of unstable modes in railway brake squeal, the objective of this paper is to objectively compare results obtained with the two models and to show how this comparison can be used to determine parameters of functional laws giving the same results as idealized contact.

1 Introduction

Simulating interactions of multiple components in mechanical assemblies is critical in many industrial applications. This requires contact and possibly friction models which have become accessible to simulation due to advances in solvers and computational power. Train brake squeal during station parking operations generates noise disturbances that can raise issues in the vicinity of stations potentially limiting train exploitation. The AcouFren project managed by SNCF (the french railway company) aims at providing, through simulation, noise indicators at early brake design stages.

Contact modeling strategies are widely documented in the literature, from which two trends are clearly found. The oldest representation is due to Signorini from the 30's, it *idealizes* a perfect contact between two ideally smooth bodies, and constrains the relative displacement of contact points. The second representation strategy is *functional* and authorizes a level of interpenetration between bodies. First measurements were performed in the 60's, from which Greenwood and Williamson [1] developed models where contact stiffness is function of the body interpenetration. State-of-the-art measurements as performed by Nogueira *et al.* [2] still show that this model can be relevant, mostly for hard surfaces. Direct ultrasonic measurement of contact

stiffnesses can also be performed. Biwa *et al.* [3] thus showed that contact stiffness is function of the contact pressure, mostly for low interfacial loading.

Physically speaking, contact between two bodies can be interpreted as the balance between their respective stiffness and asperity compression, as illustrated in figure 1. When one material is much softer than the other, like for brake systems, local compression of asperities becomes non-negligible at the macroscopic scale, generating local interpenetration of the nominal surfaces (with sometimes plastic deformation of asperity). It can then be relevant to identify a law $p(g)$ linking penetration of nominal surfaces and contact pressure.

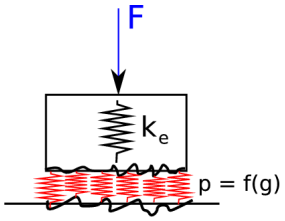

Figure 1: Representation of contact between two bodies, body stiffness and asperities

Numerically speaking, implementation of functional contact laws using continuous non linear functions of displacement is easier since classical non-linear algorithms can then be used. The ideal contact law does not feature any mechanical parameter to be identified, but its numerical implementation requires specific algorithms. Their convergence is often very sensitive and fine tuning of numerical parameters is needed. Besides, numerical convergence is often obtained with a tolerance, so that interpenetration can still occur in the results, with levels that are difficult to control.

Choosing a contact strategy is thus difficult and the general feeling is that these different contact models yield different results. The aim of this paper is to present an objective comparison of Signorini and exponential functional contact laws in application to an industrial train brake squeal simulation. Section 2 starts by presenting numerical implementation details of functional contact, based on the work of Vermot des Roches [4]. Signorini implementation is then presented, based on the work of Moirot [5]. Section 3 then demonstrates that an equivalence between both contact laws is possible, and a functional law of the exponential type is proposed. Section 4 eventually presents a validation applied to industrial railway brake models.

2 Contact formulations for squeal simulations

Squeal simulations in the frequency domain is nowadays widely deployed in industry, and is based on the *sliding perturbation* method. This was used by Moirot [5], Lorang [6] for train brake squeal applications, or by Vola *et al.* [7] to study rubber/glass instabilities in sliding steady states, and by Vermot des Roches in [4] for automotive brake squeal application. Contact formulations and adapted numerical schemes for squeal simulations are here presented.

2.1 Contact handling for finite element models

The representation of contact between two solids as formalized by Signorini is defined by a contact direction N along the outward normal at a contact point of one of the bodies (the chosen one, $S1$, is commonly called *master*, as contact forces will be evaluated on its surface). Figure 2 illustrates the contact configuration.

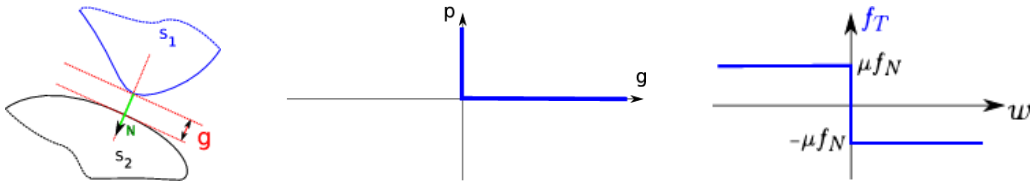

Figure 2: Contact normal (N) and gap (g) definition between solids, Signorini and Coulomb laws

The distance between the two bodies along the contact normal is called the *gap*, here noted g. The convention is that the gap is positive when contact is open, or not effective. When contact is closed, or effective, a contact pressure p exists between the bodies, applied at contact points, equal in amplitude on both solids. The contact law proposed by Signorini, illustrated in figure 2, defines the condition of non-interpenetration as

$$\begin{cases} g \geq 0 \\ p \geq 0 \\ (g).(p) = 0 \end{cases} \tag{1}$$

Quite differently, functional contact laws define a pressure-gap relationship. These can represent physical phenomena due to interaction between asperities, but have also been considered as a numerical regularization trick. Both approaches have their limitations, so that in the end the most convenient to reproduce the behavior of interest should be retained. Classical laws are illustrated in figure 3.

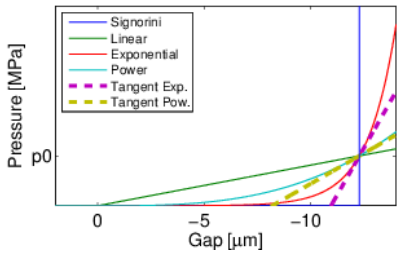

Figure 3: Classical contact laws, and their derivatives (for contact stiffness)

Numerically the gap is a linear observation of relative displacement between two surfaces along a normal, and can thus be written using an observation matrix $[C_{NOR}]$. Noting N the number of system DOF, and N_c the number of contact points, it is written with a possible gap offset $\{g_0\}$ as

$$\{g\}_{N_c \times 1} = [C_{NOR}]_{N_c \times N} \{q(u)\}_{N \times 1} - \{g_0\}_{N_c \times 1} \tag{2}$$

The force resulting from the gap-pressure relationship is then defined as an integral over the contact surface

$$\{\hat{q}\}^T \{f_N\} = \int_\Gamma \hat{u}(\hat{q}) N p(q) dS \simeq \sum_e \sum_j \{\hat{u}(\hat{q})\}^T \{N\} p(x_j, q) \omega_j^{(e)} J^{(e)}(x_j) \tag{3}$$

where f_N is the global contact force, p the contact pressure, $\hat{q}$ a virtual displacement, q the displacement, $x_j^{(e)}$ are the integration points of current element e, $J^{(e)}(x_j)$ the Jacobian of the shape transformation (surface associated to each integration point) and $\omega_j^{(e)}$ the weighting associated with the integration rule for element e.

In practice generalized contact forces can be recovered at DOF using the transpose of the gap observation (2):

$$\{f_N\}_{N \times 1} = [C_{NOR}]^T_{N \times N_c} \left\{ \omega_j^{(e)} J^{(e)}(x_j)\, p(x_j, q) \right\}_{N_c \times 1} \tag{4}$$

The Coulomb law is expressed at each contact point j as

$$\begin{cases} |f_{Tj}| < \mu |p(x_j)| \Leftrightarrow w_j = 0 \\ |f_{Tj}| = \mu |p(x_j)| \Leftrightarrow f_{Tj} = \mu |p(x_j)| \frac{w_j}{|w_j|} \end{cases} \tag{5}$$

where f_{Tj} is the friction constraint, μ the friction coefficient, and w_j the sliding velocity. Computation of the sliding velocity requires computation of differential velocities between slave and master surfaces in the plane orthogonal to the contact normal. A tangential displacement observation matrix $[C_{TAN}]$ can be used

$$\{w\}_{2N_c \times 1} = [C_{TAN}]_{(2N_c \times N)} \{\dot{q}\}_{N \times 1} = \begin{bmatrix} [C_{TAN}]_1 \\ [C_{TAN}]_2 \end{bmatrix} \{\dot{q}\}_{N \times 1} \tag{6}$$

The tangential displacement is observed in the two directions of the plane defined by the contact normal. It can be useful to distinguish observations in both directions when a natural orientation of contact forces exist. This is for example the case for this paper application as a steady sliding state exists.

Friction generalized forces can be recovered, from the local friction constraint f_{Tj} by

$$\{f_T\}_{N \times 1} = [C_{TAN}]^T_{N \times 2N_c} \left\{ \omega_j^{(e)} J^{(e)}(x_j) \; f_{Tj}(p(x_j, q)) \right\}_{2N_c \times 1} \tag{7}$$

Given a multibody system with contact interactions, the system must then verify

$$[M_{el}] \{\ddot{q}\} + [C_{el}] \{\dot{q}\} + [K_{el}] \{q\} = \{f_{ext}\} + \{f_{NL}\} \tag{8}$$

where $[M_{el}]$, $[C_{el}]$, $[K_{el}]$ are respectively the system elastic mass, damping and stiffness matrices, $\{q\}$ the displacement vector. The non linear force vector can be decomposed as the sum of contact $\{f_N\}$ and friction forces $\{f_T\}$, $\{f_{NL}\} = \{f_N\} + \{f_T\}$.

Brake squeal simulations are based on a steady sliding state, considering that all points in effective contact are sliding, thus verifying the second equation of the Coulomb law (5). A tangent model can then be derived from the steady sliding state to obtain the system stability from complex mode analysis. The same hypothesis of constant sliding for points in effective contact is used, hence the name of sliding perturbations.

Due to the priviledged sliding direction of the steady sliding state, observation matrices $[C_{TAN}]_i$ are constructed for modal analysis so that $[C_{TAN}]_1$ is along the direction of the sliding velocity of the steady sliding state at each contact point, and $[C_{TAN}]_2$ is along the orthogonal direction.

For 3D solids, Moirot [5] noted that the sliding friction tangent state also features a damping term due to the possibility for the friction force to change its orientation in vibration. A planar friction damping matrix $[C_{f2}]$ derived from the expression of friction forces thus appears, written

$$\delta f_T = [C_{f2}] \, \delta\dot{q} = [C_{TAN}]_2^T \left[\backslash \frac{\mu}{|w_j|} \omega_j^{(e)} J^{(e)}(x_j) p(x_j, q) \backslash \right] [C_{TAN}]_2 \, \delta\dot{q} \tag{9}$$

Physically, the higher the contact pressure, the more difficult the sliding direction variation. This is due to the priviledged sliding direction of the steady sliding state.

2.2 Functional contact

For functional contact formulations, classical non-linear methods can be applied, since contact-friction forces only depend on the system state. Equation (8) can then be writen using $\{f_{NL}\} = \{f_{NL}(q)\}$.

2.2.1 Functional contact statics

The Newton method, presented in figure 4, is the most classical method to resolve regular non linear statics. Difficulties in Newton resolution algorithms are mostly on the numerical side. Although mathematical convergence is obtained theoretically when the system is *regular enough*, *hard laws* like contact implementations are challenging.

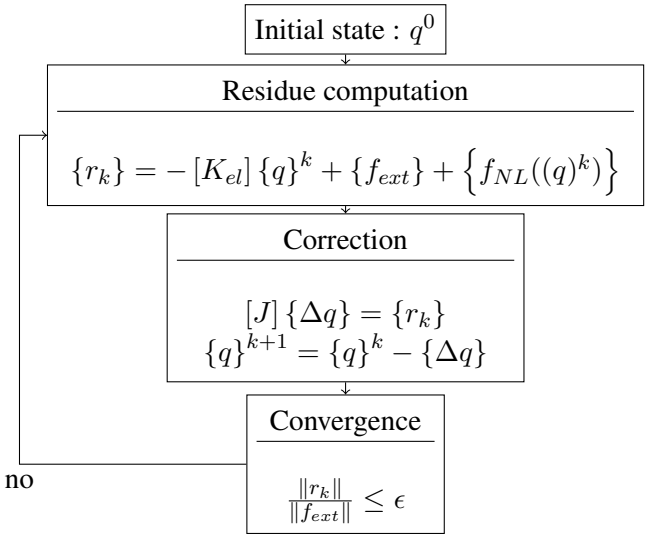

Figure 4: Implementation of a static Newton resolution scheme

The system Jacobian $[J]$ derived from (8) in statics can be written

$$[J] = [K_{el}] + [K_c(g)] \tag{10}$$

Considering a steady sliding state, the tangent friction perturbation is neglected. Noting $\omega_j J(x_j)$ the surface associated with each contact point. the tangent contact state defining $[K_c(g)]$ writes

$$\frac{\partial f_N(q+\delta q)}{\partial \delta q} = [C_{NOR}]^T \left[\backslash \omega_j J(x_j) \backslash\right] \left[\frac{\partial p(g+\delta g)}{\partial \delta g}\right] [C_{NOR}] = [C_{NOR}]^T \left[\backslash k_{cj}(g) \backslash\right] [C_{NOR}] \tag{11}$$

For hard laws, tangent state variation can be very brutal, which is a drawback of such algorithms. Indeed, when contact opening occurs in a loaded area at iteration k, tangent contact state becomes locally null, and correction can become very large (with possibly contact penetrations). Divergence can then occur quickly as the non-linear forces returned for significant penetrations lead to numerically infinite forces.

A full set of adaptations can be applied to the original Newton scheme, yielding numerous variations of quasi-Newton methods. For hard contact, cut-backs on corrections based on the norm of the mechanical residue, and controlled release on the contact part of the Jacobian for opening points are usually working and have been used here. Implementation details is key to performance, but are outside the scope of this paper.

2.2.2 Functional contact sliding perturbation formulation

Functional contact formulations are defined as function of the gap, such that a tangent state can be derived for each contact point by deriving the gap/pressure relation, illustrated in figure 3. A key aspect to note is that for similar contact pressure levels, different functional contact laws can yield very different contact stiffnesses. Contact law calibration in statics and dynamics can thus be very different.

Tangent contact stiffness has been defined in (11). Defining tangent friction states is less direct as it couples normal and tangential directions, which is typically non-symmetric. Friction expression (5) indeed shows

that a variation of contact force has a direct effect on friction force, whereas friction force variation may occur without effect on contact force.

For sliding states, friction force is explicitly defined and only depends on contact force at the same point. The tangent friction stiffness is then the tangent contact stiffness (11) scaled by the friction coefficient μ, and transfers normal displacement to planar force in the sliding direction. Since planar displacements are free for a fixed contact state, this effect is not considered for real mode computation. The tangent sliding friction coupling stiffness K_{nlf}^{slide} is thus defined as

$$K_{nlf}^{slide} = \begin{cases} 0 & \text{for real mode computation} \\ [C_{TAN}]_1^T \left[\backslash \mu k_{cj}(g) \backslash \right] [C_{NOR}] & \text{for complex mode computation} \end{cases} \tag{12}$$

Equation (11) illustrates one of the main interest of functional contact laws, which is the representaton of a contact stiffness distribution depending on contact pressure. Such variation can be non negligible for low pressures [3]. This is impossible with Signorini contact, where this pattern can only be assessed by evaluating contact opening thresholds as function of complex mode amplitudes.

2.3 Signorini, or idealized contact

Idealized contact verifying the exact Signorini condition (1) is non regular, hence the common name of *non-smooth dynamics*. $\{f_{NL}\}$ has no specific link to the displacement, and the pair $(\{q\}, \{f_{NL}\})$ has to be found using appropriate solvers.

2.3.1 Signorini statics

Solution strategies are usually based on Lagrange resolutions. The non-symmetric nature of friction requires a methodology refinement, leading to *Augmented-Lagrange* methods. De Saxcé and Feng developed the *bipotential* method [8]. Alart *et al.* presented a generalization of the Newton method adapted to Lagrange formulations introducing Gauss–Siedel like algorithms [9].

The solution chosen here was developped by Moirot [5]. It is based on the status assumption of each contact points (open/closed gap). Closed contact points generate a displacement constraint under which resolution is linear. Noting with superscript $^{(e)}$ the observation restricted to conctact points in effectively closed contact, one resolves the problem in the orthogonal subspace $\left[T^{(e)}\right]$ that verifies the constraint

$$\{q\} = \left[T^{(e)}\right] \{q_e\} \text{ with } [C_{NOR}]^{(e)} \left[T^{(e)}\right] = 0 \tag{13}$$

The subspace $\left[T^{(e)}\right]$ is unique, any $\{q_e\}$ is defined by the basis chosen for $\left[T^{(e)}\right]$ which may be arbitrary. Equation (8) can thus be rewritten in statics as

$$\left[T^{(e)}\right]^T [K_{el}] \left[T^{(e)}\right] \{q_e\} = \left[T^{(e)}\right]^T (\{f_{ext}\} + \{f_N\} + \{f_T\}) \tag{14}$$

Working with pressures is mandatory, one thus introduces an operator passing from generalized forces at DOF to local pressures at contact points $[C_{NP}]$ (based on the pseudo inversion of relation (4)), and to friction local constraints $[C_{TP}]$ (pseudo inverse operator of (7)). Contact forces verify the equilibrium and are opposed in direction and of equal norm at each observation point. Contact pressures are then expressed as

$$\{p(x_j)\} = [C_{NP}] ([K_{el}] \{q\} - \{f_{ext}\}) \tag{15}$$

and are null in $T^{(e)}$. Sliding friction forces (7) can thus be written (with $^{-1}$ denoting a pseudo inverse)

$$\{f_T\} = \mu [C_{TP}]^{-1} [C_{NP}] ([K_{el}] \{q\} - \{f_{ext}\}) \tag{16}$$

Equation (14) projected in $\left[T^{(e)}\right]$ becomes after simplification

$$\left[T^{(e)}\right]^T \left([\mathcal{I}] - \mu \left[C_{TP}\right]^{-1} \left[C_{NP}\right]\right) \left[K_{el}\right] \left[T^{(e)}\right] \{q\} = \left[T^{(e)}\right]^T \left([\mathcal{I}] - \mu \left[C_{TP}\right]^{-1} \left[C_{NP}\right]\right) \{f_{ext}\} \quad (17)$$

Assuming contact points at nodes and first order contact elements between compatible meshes, one can directly work using contact resultants. Matrices $[C_{NP}]$ and $[C_{TP}]$ are then equivalent to observation matrices $[C_{NOR}]$ and $[C_{TAN}]$ of equations (2) and (6), generated using integration rules at nodes. This simplification of implementation was used in this paper application.

It must be noted that the factor $\left([\mathcal{I}] - \mu \left[C_{TP}\right]^{-1} \left[C_{NP}\right]\right)$ is not symmetric. Direct resolution of (17) can then be challenging for large problems, like the million-DOF system presented in section 4. Use of the latest PARDISO librairies [10], implemented in SDT [11] was required here.

Contact status must be predicted, and can be updated depending on the result of (17). This is formalized by considering the group of contact nodes in effective contact in (17) at resolution iteration k, noted $\mathcal{C}_k$.

At iteration k, contact points violating Signorini conditions in the solution of (17) are classed in group $\mathcal{D}_k$ such that

$$\begin{cases} x_j \in \mathcal{C}_k, p(x_j)^k < 0 \\ \text{or} \\ x_j \notin \mathcal{C}_k, g(x_j)^k < 0 \end{cases} \quad (18)$$

Status updating allows forming a new $[C_{NOR}]^{(ek)}$ and consists in switching the status of points in $\mathcal{D}_k$,

$$\mathcal{C}_{k+1} = (\mathcal{C}_k - \mathcal{C}_k \cap \mathcal{D}_k) \cup (\mathcal{D}_k - \mathcal{D}_k \cap \mathcal{C}_k) \quad (19)$$

Iterative status correction can be resolved by an Uzawa algorithm, presented in figure 5. This method convergence has been proved without friction and by switching contact statuses one by one. Its performance is however very satisfying in the application presented, with very few iterations even for complex systems and high friction coefficients.

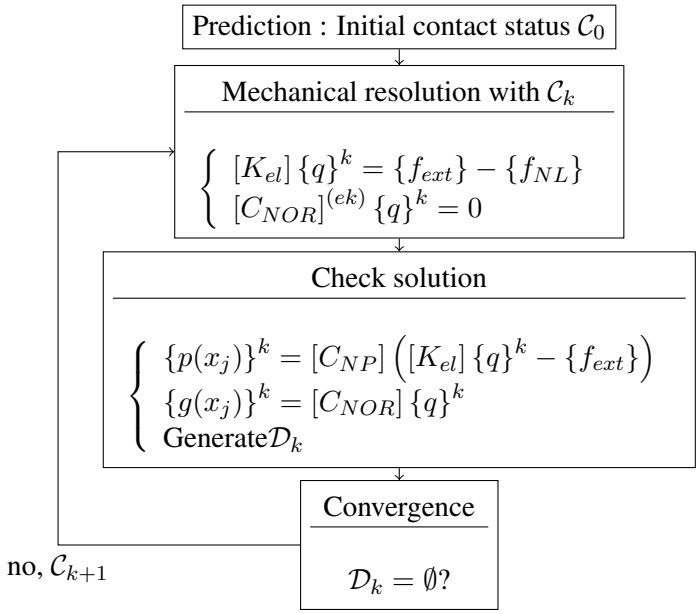

Figure 5: Implementation of an Uzawa resolution algorithm for the sliding Signorini-Coulomb problem using status

2.3.2 Signorini modal analysis

Following the exact contact condition of Signorini, the system tangent state only depends on the contact surface, materialised by $\mathcal{C}_\infty$, as presented in 2.3.1. The mechanical problem is here formulated as

$$\begin{cases} \left(\lambda^2 \left[M_{el}\right] + \lambda \left(\left[C_{el}\right] + \left[C_{f2}\right]\right) + \left[K_{el}\right]\right) \{q\} = \{f_{NL}\} \\ \left[C_{NOR}\right]^{(e\infty)} \{q\} = 0 \end{cases} \tag{20}$$

As for static resolution, projection in the subspace $\left[T^{(e\infty)}\right]$ verifying the contact constraints yields

$$\left(\lambda^2 \left[M_\mu^{(e)}\right] + \lambda \left(\left[C_\mu^{(e)}\right] + \left[C_{f2}\right]\right) + \left[K_\mu^{(e)}\right]\right) \{q_e\} = 0 \tag{21}$$

where matrices $\left[X_\mu^{(e)}\right]$ are the so-called *sliding matrices*, defined as

$$\left[X_\mu^{(e)}\right] = \left(\mathcal{I} - \mu \left[C_{TP}\right]^{-1} \left[C_{NP}\right]\right) \left[T^{(e\infty)}\right]^T \left[X_{el}\right] \left[T^{(e\infty)}\right] \tag{22}$$

3 Definition of an exponential contact law

The two contact models presented in section 2 are physically limited, so that the choice of one or the other should be based on the ability to reproduce specific behavior and on the performance of algorithms used to resolve equations. The objective of this section is to demonstrate how the ability to reproduce specific modal behavior can be used to calibrate the parameters of an exponential pressure/gap law that reproduces the idealized behavior.

3.1 The clamped/sliding block

Railway industry pads can be of different shapes and materials, the sample pad shown in figure 6 is used as an example here. A single friction block (made of friction material), solidar to a metallic ring making the link to the backplate, is extracted for the illustration. The friction material has a non-negligible loss-factor. Here, this damping is modelled by a material Rayleigh damping for easy compatibility for transient simulations, even though better models [12] are probably needed.

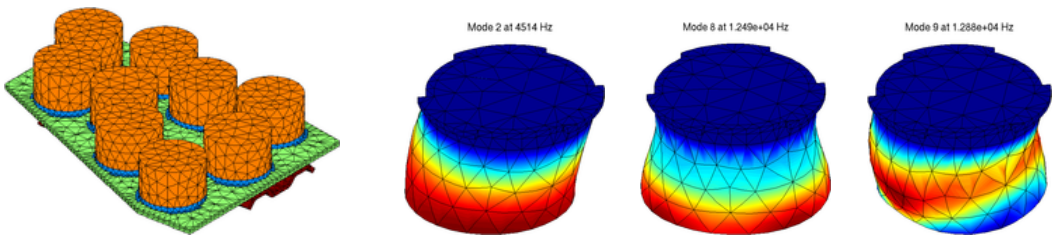

Figure 6: Left: A sample railway braking pad. The friction blocks in orange are linked to the backplate in green, using rings in blue. A dovetail joint (in red) fixes the pad in the brake rig. Right: Sample block modes in clamped/sliding conditions with ideal contact for a ring fitted block

When computing steady sliding states and sliding perturbations, the friction blocks effective contact area is supposed to be fully sliding (although some contacts can be opened). A sample demonstration of the blocks behavior is thus to consider them in clamped/sliding condition. Ideal contact condition is materialized in this case by clamping normal displacements of the friction block bottom side. Figure 6 shows some modes associated to the pad block in such conditions.

To demonstrate the effect of contact stiffness (possibly derived from a functional contact law), normal spring elements with variable stiffness are added to the blocks bottoms instead of clamping. The previous case would then correspond to a spring with infinite stiffness.

Figure 7 presents complex mode frequency and damping results of the clamped sliding block as function of contact stiffness. An *S-shaped* frequency evolution can be observed. Saturation occurs around $10^4 MPa$, after which frequencies are equivalent to an ideal contact implementation.

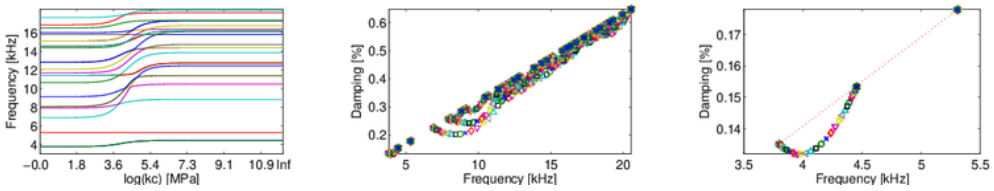

Figure 7: Frequency (left) and damping (middle) evolution as function of the contact stiffness applied to the lining block of the brake pad. Right: zoom in on the first modes.

Mode damping evolution as function of contact stiffness can be observed in figure 7. Damping rates increase with frequency as a consequence of the stiffness proportionality coefficient used to form the material Rayleigh damping matrix.

For low contact stiffnesses, ground coupling is small and the friction block behaves as free, that-is-to-say the whole strain energy is located in the block. Damping ratio of the clamped/sliding block is thus linked to the damping ratio of the block itself. The same observation can be done for high contact stiffnesses, when coupling is strong and the friction block behaves as clamped. The expected damping ratio increase is obtained regarding the frequency increase, materialized by the dotted line in figure 7right.

In the curve inflection area, a non negligible strain energy is located in the coupling springs, so that a non negligible part of the total system strain energy is outside the friction block. The damping ratio thus varies non linearly, and can even decrease when coupling becomes non negligible while still being low. This observation is very general regarding impact of components strain energy distribution in damping of assemblies. More detailed illustrations of this effect can be found in [12].

3.2 Exponential contact law definition

As a large variety of functional contact laws could be calibrated, one decided here to focus on the exponential type. This choice is based on the expected transient behavior, where contact opening transitions and penetration saturation effects also need to be properly represented for a potentially large range of pressures. Numerical results obtained in [4] with such law were satisfying.

Given $\{g\}$ the gap vector (opposite of the penetration), obtained from an observation of the relative displacement of both surfaces along the local contact normal, pressure $\{p\}$ is defined as

$$\{p\} = p_0 e^{-\lambda\{g\}} \tag{23}$$

The exponential law has two parameters p_0 and λ, whose effect on contact behavior is illustrated in figure 8. To interpret these curves, values have to be observed as function of a reference force level, conceptually named F. Horizontal intersections are thus iso-values regarding system loading outside the contact area.

Parameter p_0 only drives the curve offset, thus the level of gap obtained for a given force. Identification of this parameter can be obtained if measurements of surface rougthness are accessible, providing acceptable values of interpenetrations. In this paper, coefficients are only numerically calibrated so p_0 can be set arbitrarily. Choosing a p_0 such that significant contact pressures are obtained for closed (or negative) gaps, simplifies implementation and allows easier physical interpretations.

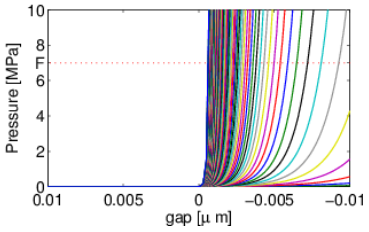

(a) $p_0 = 10^4, \lambda \in (10^2; 10^{10}) m^{-1}$

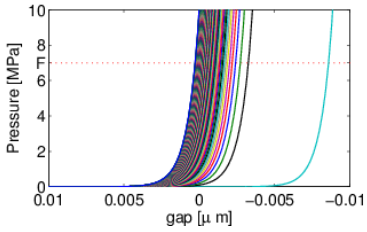

(b) $\lambda = 1.3.10^9, p_0 \in (10^2; 10^7) Pa$

Figure 8: Exponential contact law evolution as function of its parameters

Parameter λ impacts contact stiffness at a given force level, the higher, the stiffer. This parameter itself can thus be updated to choose a contact stiffness that complies with the fact that the frequencies in clamped/sliding conditions are converged towards the perfect contact behavior. Looking at the diagrams of figure 7, target contact stiffnesses values can be pin-pointed in figure 9.

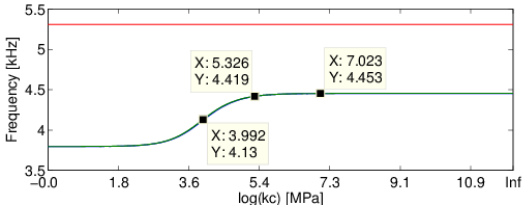

(a) Stiffness identification

Target stiffness [MPa]	$\lambda[mm^{-1}]$
10^7	$4.28\ 10^7$
$10^{5.3}$	$9.64\ 10^5$
10^4	$4.83\ 10^4$

(b) Table 3.2 : k, λ correspondances

Figure 9: Identification of target contact stiffnesses of the clamped/sliding block, and identified λ

For calibration, the level of contact pressure generated by the system must be evaluated, either by using a status implementation or by choosing a linear contact law for a preliminary computation, or by exploiting the system command (this was done here). Noting p_1 the reference pressure, contact pressure and contact stiffness $k_c(g)$ (first order derivative of contact pressure) expressions yield

$$\begin{cases} p_1 = p_0 e^{-\lambda g} \\ k_c(g) = \lambda p_0 e^{-\lambda g} \end{cases} \tag{24}$$

The product λg can be substituted in the first equation of (24) so that

$$\lambda = \frac{k_c(g)}{p_1} \tag{25}$$

Choosing a target value of $k = 10^7 MPa$ in figure 9, and knowing that the contact force command on the TGV brake system is here of $5kN$ over a surface of $21.4\ 10^3 mm^2$, one obtains $\lambda = 4.28\ 10^7 mm^{-1}$. Higher values could also be used for security margin regarding system variability. It must however be kept in mind that values with too high stiffness may alter numerical conditioning of the stability problem.

For comparison purposes, a converged value $kc = 10^{5.3} MPa$ at the limit, and a non converged value $kc = 10^4 MPa$ will also be tested. Correspondances between λ and target stiffnesses are reported in table 3.2.

4 Application to industrial railway brakes

The french high speed train, TGV, features 4 disc brake systems on each axle, as presented in figure 10. A single brake system is here modelled by finite elements on which subassemblies (the disc, rig and pads) have

been updated as part of the AcouFren project. The full model is free-meshed using second order ten nodes tetraedrons, yielding between 500,000 and 1,000,000 DOF depending on the fitted pad model.

The mesh is kinematically positioned depending on the pad thickness to have zero gap at rest. Disc sections underlying the pads are remeshed to obtain compatible contact interfaces. Braking force is applied by an actuator at the system rear, which translates the pad holder towards the disc. The translation is achieved kinematically by the rotations of levers and rods, constituting the brake rig.

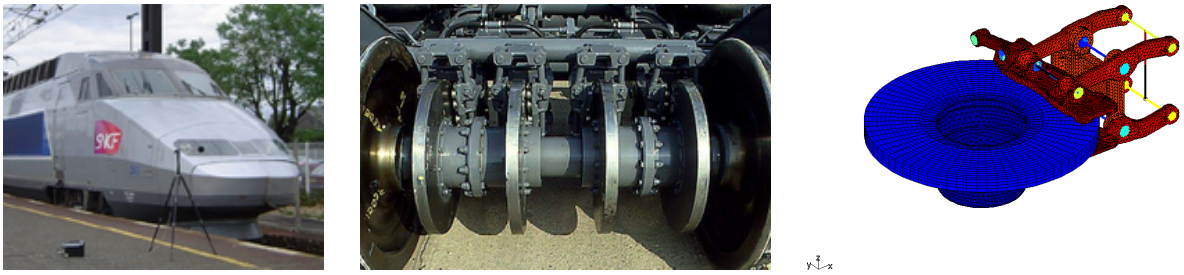

(a) TGV (b) 4 TGV discs on a TGV axle (c) TGV brake FEM

Figure 10: The TGV brake system

The illustration will focus on complex mode evaluation for station parking operations. Comparisons between calibrated exponential laws, defined in section 3.2 and the idealized contact implementation are presented for steady sliding solutions in section 4.1 and complex modes in section 4.2.

4.1 Steady sliding simulations

A contact force command of $5kN$ is applied by the actuator. Figure 11 presents global steady sliding solution with ideal contact implementation. Levels of displacement and contact force resultants are presented. Largest displacements are seen by the lever with values around $140\mu m$. Contact force distribution greatly varies over the contact surface. Friction blocks of the front end are the most loaded, unloading of the trailing end seems complicated and is function of the pad holder fixations.

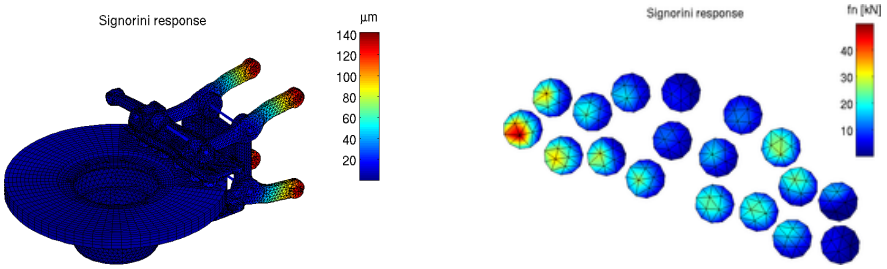

Figure 11: Steady sliding state absolute displacement of a TGV brake using Signorini contact implementation, contact resultant at nodes of the disc top side

Static results are compared between Signorini contact and the family of exponential contact laws defined in table 3.2. In the following, *contact nodes* define nodes of the mesh in the contact area, while *Gauss contact points* define the Gauss contact integration points used for functional contact implementation.

Figure 12 presents contact results in terms of pressure and gaps. Points with gaps opened at contact nodes are presented in figure 12a. It can be seen that no global difference rises for these displacements. Although contact pressure from an exponential law is strictly positive, exponential decay as function of opening is sufficient not to alter the behavior of unloaded contact points.

Figure 12b presents gap results for closed contact. Great differences can here be observed, the softer the law, the deeper the penetration. Penetration levels seem reasonable compared to global displacements for converged λ values only.

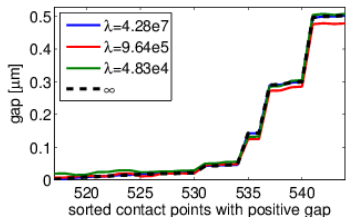

(a) Gaps at open points

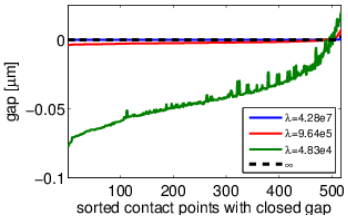

(b) Gaps at closed points

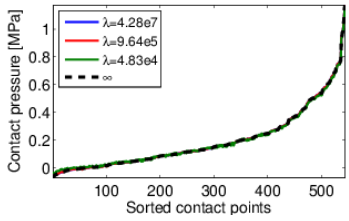

(c) Contact pressure at nodes

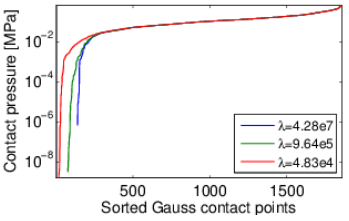

(d) Contact pressures at Gauss points

Figure 12: Comparative gaps and contact pressures between Signorini and exponential laws resuls.

Figure 12c presents contact pressure at contact nodes. Contact pressures at the interface are here computed *a posteriori* from displacements to allow comparison between implementations, using a nodal resultant to nodal pressure operator ($[C_{NP}]$ in (15), integrated at Gauss points). Opened contact points will thus show negative pressures at the interface, which would correspond to depressions on a membrane. Such observation shows that pressure levels seen by the structure outside the interface are very similar. Forces transmitted by the interface are naturally recovered in all cases, which is physically natural.

Global results in figure 12c can be put into perspective with the local results of figure 12d. Contact pressures are here plotted at the Gauss contact points for the functional laws only. Clear differences occur for low pressure areas, with a convergence pattern as function of λ. Such fluctuations for very low pressures are however not percieved by the structure.

Figure 13 presents absolute differences in displacement between the Signorini response and functional contact laws. It can be seen that for all cases, maximum differences scale in nanometers are a thousand times smaller than displacement scale.

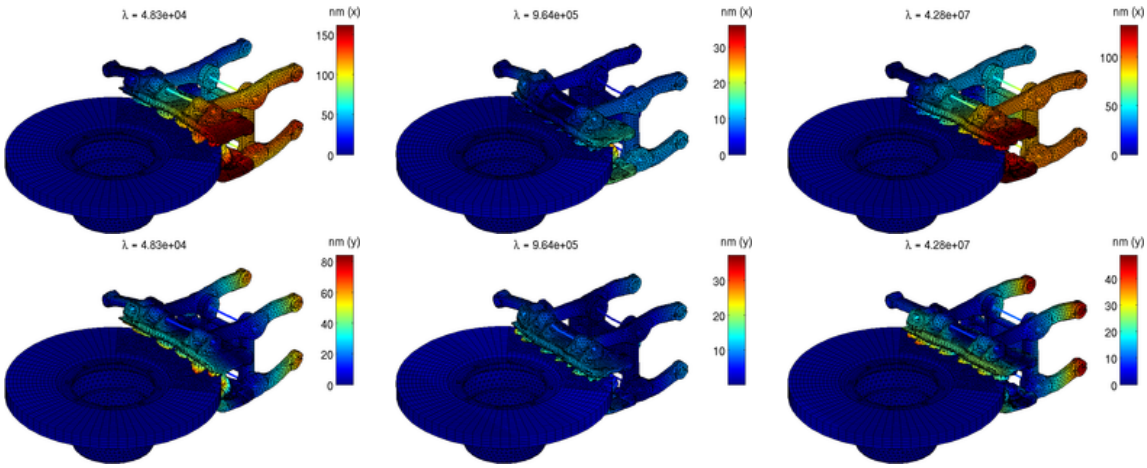

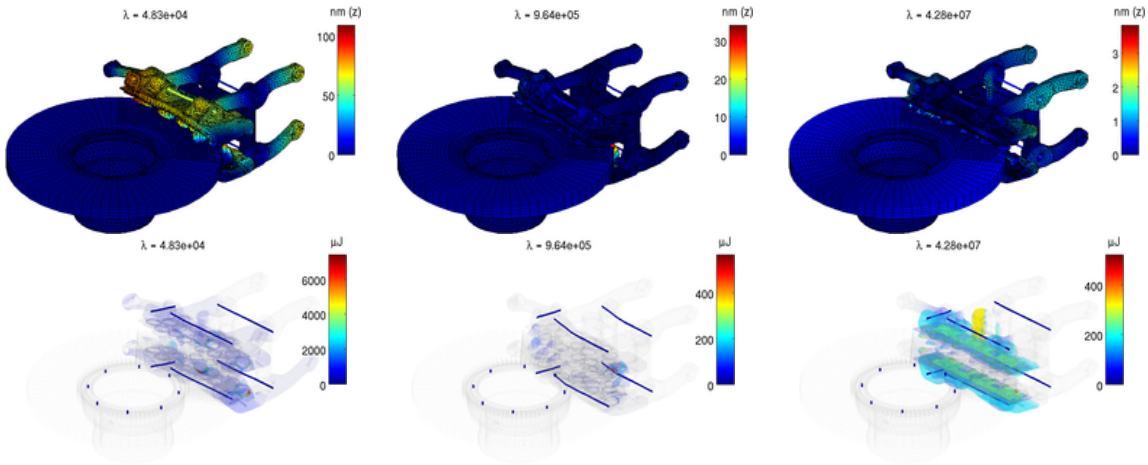

Figure 13: Absolute displacement differences in nanometers between Signorini and functional static results, from top to bottom along the x, y and z axis, from left to right in increasing λ. Strain energy densities of differential displacements are presented for elements with highest levels only

Orientation axis references are provided in figure 10. Convergence in the z axis is direclty linked to gap observations of figure 12b, and is clearly established as function of λ. Displacements in the x, y plane are linked to the rig deformation, depending on the pad holder displacement. Larger differences can here occur, with very limited strain energy errors for converged cases. Although static displacement seems better for the middle law, contact stiffness distribution is not as good, as will be discussed in section 4.2.

4.2 Sliding perturbation results

Complex modes are directly computed based on the formulations of section 2. Stability diagrams are presented in figure 14 for 500 modes, providing a frequency bandwidth of $0 - 10kHz$. The global stability diagram of figure 14b shows the effect of material Rayleigh damping, with very large damping ratios on the first modes (mass factor) and an average damping ratio linear increase with frequency (stiffness factor).

The first four most unstable modes are plotted in figure 14a and 14c. Modes 27 and 69 are pad/disc coupling modes, with effective displacement of the pad holder. Modes 81 and 59 are *planar* modes, instability coming from friction block modes (possibly coupled with in-plane disc modes). No unstable modes of the global structure were found for high frequencies in this configuration – Rayleigh damping coefficients still needed experimental fitting in this study's model.

Globally, stability diagrams fit relatively well for all exponential calibrations. Larger differences are obvious for the soft value, highlighting a convergence as function of λ. Zooms in are provided in figures 14d, 14e and 14f. Structure modes (with clear displacement of the brake rig) are in the $2kHz$ range, and show correct fittings, although the soft law presents some peculiarities.

Modes in the $5.5kHz$ and $9kHz$ ranges mostly feature friction block modes. Slight differences between *converged* λ values and Signorini are mostly due to contact stiffness variation of low contact pressure areas. A near perfect match stability diagram is here only obtained for the hardest value of λ.

Comparison between unstable mode shapes with MAC is finally presented in figures 14g,h,i. Due to the large number of modes computed and model size, each modal basis weights over 3 GBytes, making direct comparisons difficult. Unstable modes are of higher interest due to their propensity to generate squeal, hence the choice to compare only these shapes, with a detection threshold set under a damping ratio of $-10^{-3}\%$.

Convergence as function of λ is well observed regarding the number of detected unstable modes and their shape correlation, figure 14i displays a squared matrix with unit diagonal. More unstable modes with no equivalent in the Signorini results are found for the two softest λ values.

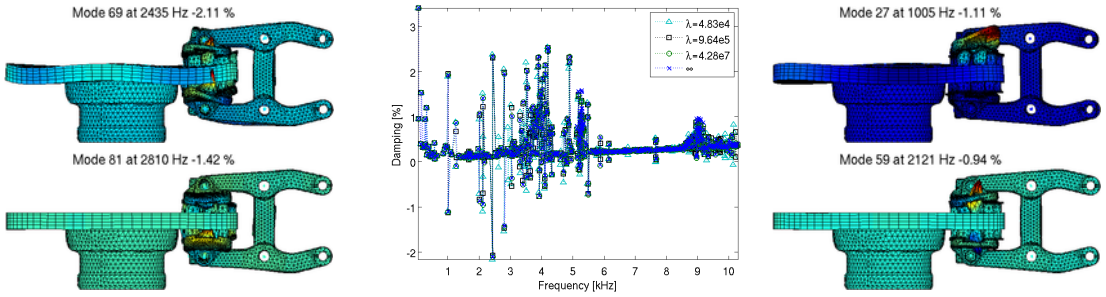

(a) Most unstable modes 1 and 2 (b) Global stability diagram (c) Most unstable modes 3 and 4

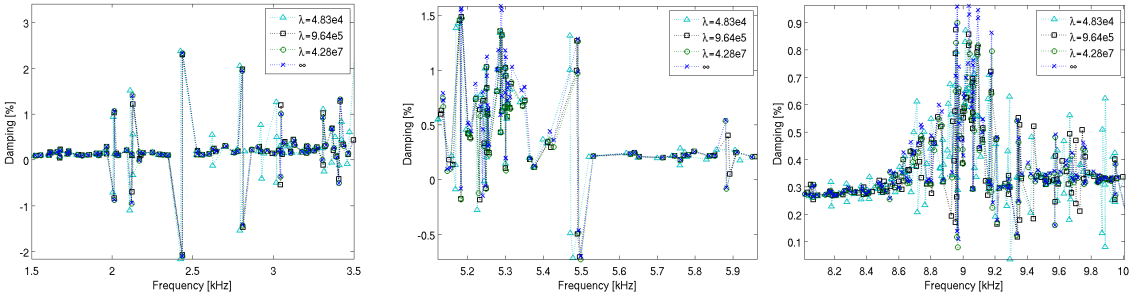

(d) Zoom around $2kHz$ (e) Zoom around $5.5kHz$ (f) Zoom around $9kHz$

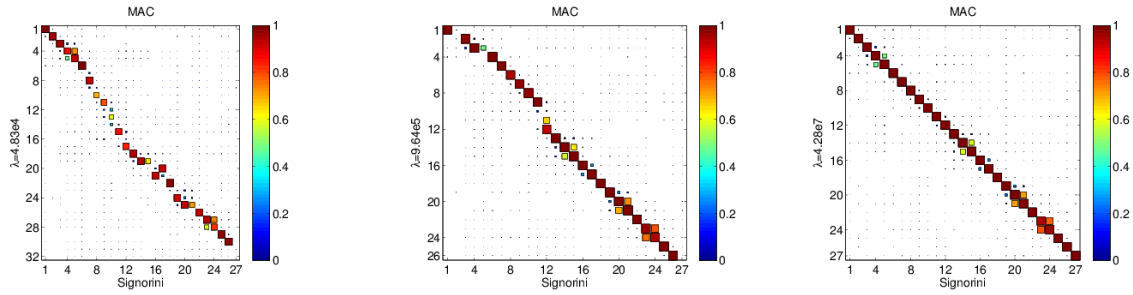

(g) $\lambda = 4.83.10^4$ (h) $\lambda = 9.64.10^5$ (i) $\lambda = 4.28.10^7$

Figure 14: Stability diagrams of Signorini solutions and functional law solutions. Most unstable TGV modes, zooms around frequency ranges of interest and unstable modes ($\zeta \leq -10^{-3}\%$) MAC between Signorini and exponential laws solutions

5 Conclusion

Simulation of structure-structure interaction is important in many industrial applications, requirering performant implementation of relevant contact models. Physically, transmission of contact forces between structures should naturally show correct contact pressures independently of the contact law.

Idealized contact avoids identification of physical parameters, but also lacks representation of contact stiffness variation as function of contact pressure. Functional laws require parameters, which can be very difficult to obtain experimentally. An exponential law was retained for its advantage of a quick decay of contact forces for opened gaps, while keeping relevant saturation patterns. For this law it was shown here that numerical calibration can be performed by considering the apparent stiffness at interfaces.

For the computation of complex modes of squealing brakes using the sliding perturbation framework, ideal and exponential contact were then shown, for properly calibrated parameters, to give nearly identical results in pressures and predicted modes. With two models leading to equivalent results, choices can then focus on implementation performance. An ongoing extension of the work presented here is the use of this benchmark to analyze transient simulations using methods presented in [4].

Acknowledgements

The authors wish to thank the members of the AcouFren project, SNCF, IFSTTAR-LTE, SDTOOLS, VIBRATEC, ENPC, ECL-LTDS, ALSTOM TRANSPORT, BOMBARDIER, FAIVELEY, and funder ADEME under the convention 0966C0281.

References

[1] J. A. Greenwood and J. B. P. Williamson, "Contact of nominally flat surfaces," *Proceedings of the Royal Society of London. Series A, Mathematical and Physical Sciences*, vol. 295, no. 1442, pp. pp. 300–319, 1966.

[2] I. Nogueira, F. Robbe-Valloire, and R. Gras, "Experimental validations of elastic to plastic asperity-based models using normal indentations of rough surfaces," *Wear*, vol. 269, no. 11 12, pp. 709 – 718, 2010.

[3] S. Biwa, S. Hiraiwa, and E. Matsumoto, "Stiffness evaluation of contacting surfaces by bulk and interface waves," *Ultrasonics*, vol. 47, no. 1 4, pp. 123 – 129, 2007.

[4] G. Vermot des Roches, *Frequency and time simulation of squeal instabilities. Application to the design of industrial automotive brakes*. PhD thesis, École Centrale Paris, CIFRE SDTools, 2010.

[5] F. Moirot, *Etude de la stabilité d'un équilibre en présence de frottement de Coulomb*. PhD thesis, Ecole Polytechnique, 1998.

[6] X. Lorang, *Instabilité vibratoire des structures en contact frottant: Application au crissement des freins de TGV*. PhD thesis, Ecole Polytechnique, 2007.

[7] D. Vola, M. Raous, and J. A. C. Martins, "Friction and instability of steady sliding: squeal of a rubber/glass contact," *Int. J. Numer. Meth. Engng.*, vol. 46, pp. 1699–1720, 1999.

[8] G. D. Saxcé and Z. Q. Feng, "The bipotential method: A constructive approach to design the complete contact law with friction and improved numerical algorithms," *Mathematical and Computer Modelling*, vol. 28, no. 4-8, pp. 225–245, 1998. Recent Advances in Contact Mechanics.

[9] F. Jourdan, P. Alart, and M. Jean, "A gauss–siedel like algorithm to solve frictional contact problems," *Comput. Methods Appl. Mech. Engrg.*, vol. 155, pp. 31–47, 1998.

[10] O. Schenk and K. Gärtner, "Solving unsymmetric sparse systems of linear equations with pardiso," *Future Generation Computer Systems*, vol. 20, no. 3, pp. 475 – 487, 2004. Selected numerical algorithms.

[11] E. Balmes, J.-P. Bianchi, and G. Vermot des Roches, *Structural Dynamics Toolbox 6.4 (for use with MATLAB)*. SDTools, Paris, France, www.sdtools.com, October 2011.

[12] J.-P. Bianchi, E. Balmes, G. Vermot des Roches, and A. Bobillot, "Using modal damping for full model transient analysis," in *Proceedings of the International Conference on Advanced Acoustics and Vibration Engineering (ISMA)*, 2010.